atmosphere

MDPI

Article

Performance Evaluation of Sub-Grid Orographic Parameterization in the WRF Model over Complex Terrain in Central Asia

Huoqing Li [1,2], Junjian Liu [1], Hailiang Zhang [1], Chenxiang Ju [1,*], Junjie Shi [3,*], Junlan Zhang [3], Ali Mamtimin [1] and Shuiyong Fan [2]

1 Institute of Desert Meteorology, China Meteorological Administration, Urumqi 830002, China; lihq@idm.cn (H.L.); liujj@idm.cn (J.L.); zhanghl@idm.cn (H.Z.); ali@idm.cn (A.M.)
2 Institute of Urban Meteorology, China Meteorological Administration, Beijing 100089, China; syfan@ium.cn
3 Xinjiang Meteorological Observatory, Urumqi 830002, China; zjl_0997@sina.com
* Correspondence: jucx@idm.cn (C.J.); belongtab@163.com (J.S.); Tel.: +86-181-1912-1606 (C.J.)

Received: 6 October 2020; Accepted: 26 October 2020; Published: 28 October 2020

Abstract: The terrain of Central Asia is complex and rugged over mountains. Consequently, wind speed is overestimated over mountains and plains when using the Weather Research Forecast (WRF) model in winter. To solve this problem, three different simulations (named as control simulation (CRTL), gravity waves (GWD), and flow-blocking drag (FBD), respectively) were designed to investigate the impact of sub-grid orography (gravity waves and flow-blocking drag) on wind forecasts. The results illustrated that near-surface wind-speed overestimations were alleviated when sub-grid orographic drag was used in GWD, though the upper-level wind fields at 500 hPa were excessively reduced compared to CRTL. Thus, we propose eliminating the gravity wave breaking at the upper level to improve upper-level wind underestimations and surface wind speeds at the same time. The sub-grid orographic drag stress of the vertical profile over mountains was reduced when only the flow-blocking drag was retained in FBD. This alleviated underestimations of the upper-level wind speed and near-surface wind, which both have the same positive effects as the gravity wave and flow-blocking total. The mean bias and root mean squared error reduced by 32.76% and 9.39%, respectively, compared to CRTL. Moreover, the temperature and specific humidity in the lower troposphere were indirectly improved. The results of the study demonstrate that it is better to remove sub-grid orographic gravity wave drag when using the gravity wave drag scheme of the WRF model.

Keywords: flow-blocking drag; WRF; complex terrain; gravity waves drag; Central Asia

1. Introduction

The effects of orography can be represented by various means in large-scale models of the atmosphere, and their inclusion is crucial for successful simulations and forecasts of weather and climate [1]. An analysis of medium-term numerical forecasts in the 1980s found that upper-troposphere wind speeds in the northern hemisphere were significantly overestimated in winter. This system has an effect on predictions of sea-level pressure, underlying wind fields, and altitude. It has been shown that high wind-speed bias in wintertime through mountains is mainly caused by neglecting orographic drag effects [2]. In recent years, some parameterizations attempted to represent more profound additional drag exert on atmospheric circulation, and the sub-grid scale orographic parameterization scheme was proposed to solve orographic features and has been widely applied in atmospheric models [3]. In general, sub-grid orographic drag is classified into three types: drag from gravity waves (GWD), low-level wave breaking (LLB), and flow-blocking drag (FBD). Gravity waves are generated by flow

over mountains that propagates vertically upward to not only troposphere, but also mesosphere and thermosphere, and produces drag when breaking [4–7]. LLB and trapped downstream lee waves can enhance drag in the lower troposphere. FBD is forced by flow blocked on the mountain flanks or flowing around mountains under upstream stable conditions, providing drag near the surface where the blocking occurs [8]. FBD exerts an important effect on the circulation of the low-tropospheric atmosphere over mountains in complex terrain. It directly controls wind fields, which further modulate water vapor and energy transport. FBD parameterizations improve the wind fields over the lower troposphere and indirectly affect temperature and others fields [9].

The Weather Research Forecast (WRF) model parameterizes sub-grid gravity wave drag and FBD together as dynamical processes [1,9–11] to reduce the bias in wind speeds over complex terrain. This improves the performance of winds forecast at 10 m [12]. However, GWD generally provides large-scale drag at upper levels when the waves break, and this can reduce the upper-level (the upper level is upon 500 hPa; on the contrary is low levels) wind fields circulating through the mountains [13]. Moreover, vertical momentum transfer is also affected [14,15], and precipitation is indirectly affected [16]. When GWD stress and FBD stress are calculated as the sum stress of orography in the WRF model, upper-levels winds are excessively reduced. Such phenomena exist in the Tibetan Plateau when using the regional model [17]. The WRF model suffers from high-surface wind-speed bias over plains and valleys, limiting its use for several applications [12].

We evaluated the performance of sub-grid orographic parameterizations to determine which one is more suitable for the complex terrain of Central Asia. Three different simulations were designed: a simulation that included GWD (the sum of GWD and FBD), a simulation of FBD, and a control simulation (CRTL). The differences between the GWD and FBD sub-grid orographic schemes were investigated using data from one winter month in the complex terrain of Central Asia. The simulations were examined against observation data from surface stations and radio soundings of the China Meteorological Administration. The distribution of vertical wind speed, drag stress near the surface, and vertical profiles over mountains generated from orography were compared and analyzed. Further, we discuss how to reduce upper-level wind underestimations based on this dynamic mechanism.

2. Model and Simulation Design

2.1. WRF Model

The model used in this study is version 3.8.1 of the WRF, which was recently developed from the ongoing Mesoscale Model (MM5). The fully compressible conservative form of the nonhydrostatic atmospheric model is designed for both research and operational numerical weather prediction (NWP) applications. The WRF is suitable for use in a wide range of applications across scales ranging from meters to thousands of kilometers. The WRF is a fully compressible non-hydrostatic model with a horizontal lattice in Arakawa-C format, a vertical coordinate system of power quality, and Euler center-based on-terrain following. Physical parameterization schemes can be selected in the model, including microphysics, cumulus, planetary boundary layer, and land surface processes. The WRF modeling system includes the WRF Pre-Processing System (WPS), the Advanced Research WRF (ARW), and the WRF data assimilation (WRFDA) and post-processing systems. The WPS contains the initial data used to define the simulation domain, interpolate terrestrial data (including ground vegetation, terrain, soil type, and land use), and horizontally interpolate the initial data into the simulation domains [18,19].

2.2. Flow-Blocking Drag

The WRF model includes the effects of the GWD from sub-grid scale orography. This not only treats the traditional upper levels wave breaking due to the orographic variance from mountains (non-dimensional), but also the enhanced lower troposphere wave breaking due to drag by flow blocked on mountain flanks near the surface (FBD). The upper levels and near-surface drag are

calculated as the sum of GWD when using the ACM2 planetary boundary layer scheme with the option of gravity wave drag. The GWD parameterization has been extended to include the effects of orographic anisotropy. This considers the orographic direction (OD), which is equivalent to the horizontal aspect ratio of the orography, formulated as

$$\mathrm{OD} = \frac{L_\mathrm{g}}{L_\mathrm{d}} \tag{1}$$

where L_g is the effective orographic length, which represents the subgrid-scale mountain width in the direction of low-level wind measured at the critical orographic height. Further, L_d denotes L_g for the cross-wind direction. The Froude number is the factor to determine the GWD stress at a reference level (the level is a assumed relatively height surface and not influenced by other force) [20], and is then redefined through multiplication with OD as follows:

$$Fro = h\frac{N_0}{U_0}\mathrm{OD} \tag{2}$$

where h is the orographic height, which is defined as the standard deviation of sub-grid scale orography (SSO); N_0 is the low-level Brunt–Väisälä frequency; and U_0 is the low-level horizontal wind speed. The GWD stress (τ_GWD) at the reference level is given as follows:

$$\tau_\mathrm{GWD} = \rho_0 Eh\frac{m}{\lambda}G\frac{|U_0|^3}{N} \tag{3}$$

$$E = (OA+2)^{C_\mathrm{E}Fr0/Frc}\cdot m = (1+Lg)^{(OA+1)}\cdot \mathrm{G} = \frac{Fr_0^2}{Fr_0^2 + C_G OC} \tag{4}$$

where ρ_0 is the low-level density; E is the enhancement factor for representing the nonlinear enhancement of drag due to low-level wave breaking, which is calculated by the orographic asymmetry (OA), representing the shape and location of subgrid-scale orography relative to the grid and the Fr_0 normalized by its critical value (Fr_c = 1); m is the amount of subgrid-scale orography; λ is the effective grid length; G is an asymptotic function that provides a smooth transition between the nonblocking and blocking cases and includes the effect of orographic convexity (OC) corresponding to the vertical orographic aspect ratio; and C_E and C_G are set to 0.8 and 0.5, respectively, based on the mesoscale simulation results from Kim and Arakawa [10]. A more detailed description is given by Kim and Doyle [1]. The GW stress is the same as that of Hong et al. [21], except for the Fr_0, which includes the effect of OD and a free parameter, λ. In Hong et al., λ was practically set to the grid length with a minimum limit of 50 km. In our study, it is set to twice the grid length without the limit. The updated λ has little effect on short- and medium-range forecasts but gives slightly better seasonal forecasts. The FBD effects are included in the gravity wave drag parameterizaion. The flow-blocking stress is given as follows:

$$\tau_\mathrm{FBD} = \frac{1}{2}\rho_0\frac{m}{Lx^2}C_\mathrm{d}L_\mathrm{d}h_\mathrm{b}|U_0|^2 \tag{5}$$

where L_x is the grid box area, C_d is the bulk drag coefficient of order unity, L_d is the grid length in the cross-wind direction, and h_b is the height of the blocked layer.

2.3. Simulation Setup

Comparative simulations were performed using WRF3.8.1 without a gravity wave drag scheme (CRTL), with gravity wave drag (including both gravity wave breaking and flow blocking) (GWD), and with flow blocking exclusively (FBD only). The sub-grid orographic effect is significant mainly in winter or with a stable atmospheric layer. We focus on period of atmospheric stratification stable, so the simulation period was selected as January 2019. The simulation nested domain and topography are illustrated in Figure 1. Domain 1 covered Central Asia and China with complex terrain,

including the Tibetan Plateau, the Tianshan Mountains, and the Iran Plateau. Moreover, the Central Asian region includes Xinjiang's upstream weather area as the main source of water vapor transport. Domain 2 covered Xinjiang and its western mountainous areas, where many synoptic observation stations are distributed. The model was vertically divided into 50 layers, and the configuration of the parameterization schemes was as follows: the micro-physics scheme from the WSM6 [21] and the cumulus scheme from Kain–Fritsch [22], D02 domain without a micro-physics process, the RRTMG scheme for both long-wave and short-wave radiation [23,24], the planetary boundary layer scheme is the YSU [25] scheme with a gravity wave scheme [9], and the land surface scheme is the Noah land surface model [26]. The model was initialized and driven by NCEP FNL reanalysis data, hourly forecasts, and a 24 h forward cycle. Details of the simulations used in this work are provided in Table 1.

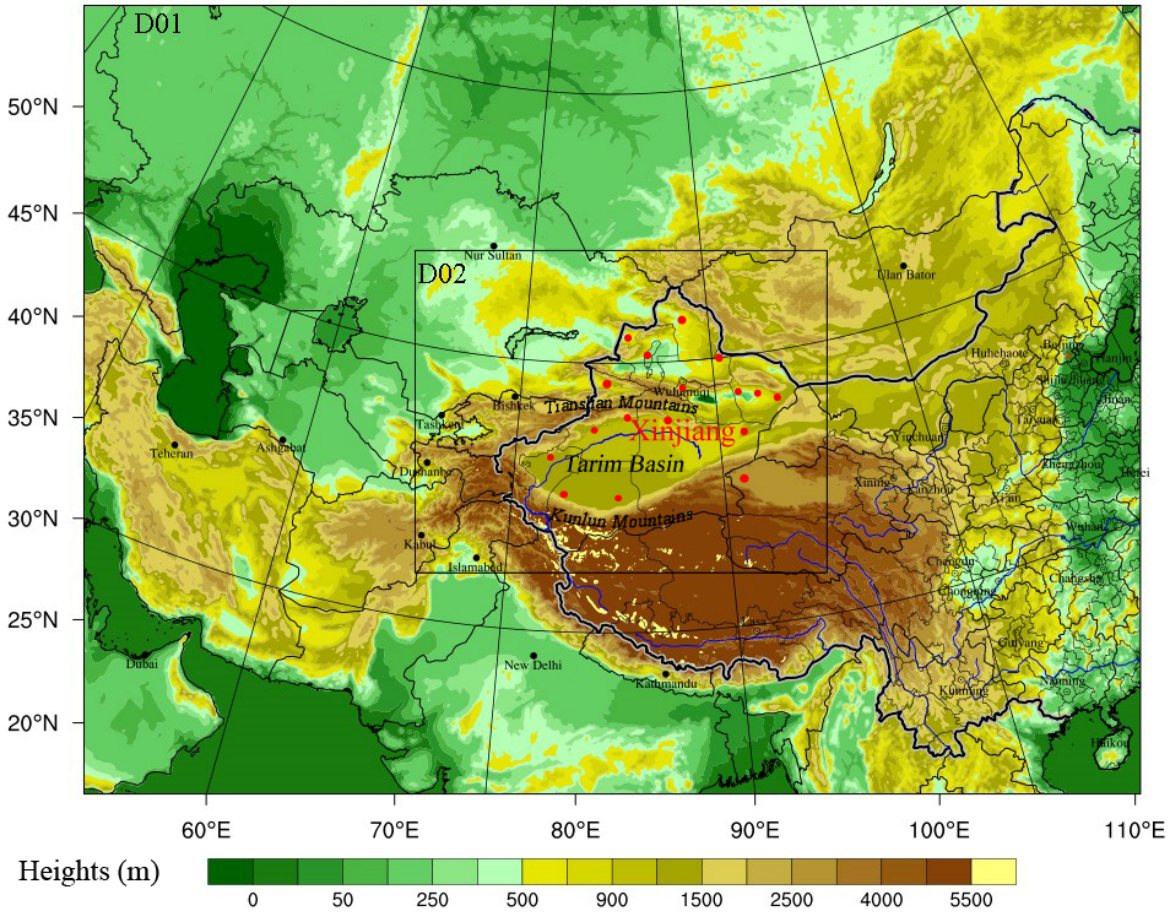

Figure 1. Two nested domains and topography (the red dots show radio sounding stations).

Table 1. Detailed parameterization schemes of three simulations.

Simulation	Parameterization Schemes (Parallel)	Sub-Grid Orographic Drag
CRTL	micro-physics:WSM6; cumulus: Kain–Fritsch	no gravity wave drag scheme
GWD	long-wave: RRTMG; short-wave: RRTMG	gravity wave drag
FBD	planetary boundary layer: YSU; land surface: Noah	only flow-blocking drag

2.4. Observational Data and Metrics of the Evaluation

We determined the direct impact of sub-grid orographic parameterizaion on wind fields and the indirect effect on 2 m air temperature and specific humidity. The effects of the simulations were investigated base on hourly observation data from 105 synoptic stations and 14 radio sounding stations in Xinjiang. The distribution of the stations is shown in Figure 1. The evaluation elements

included surface wind speed, 2 m air temperature, relative humidity, vertical upper-level wind speed, and temperature. The evaluations used in this study were the mean bias (MB), mean absolute bias (MAE), and root mean squared error (RMSE).

3. Results

3.1. SSO Analysis and GWDO Distribution

Central Asia includes many mountain ranges, including the Tibetan Plateau, Tianshan Mountains, Altai Mountains, and the Iranian Plateau, where terrain is complex and orographic variance is large. Orographic variance is calculated based on high-resolution elevation data. It represents the heterogeneity of sub-grid orography and exerts gravity wave drag. The spatial distribution of sub-grid orographic variance in Central Asia is illustrated in Figure 2. Large orographic variance is mainly located around the mountains that are steep and rugged, such as the Tibetan Plateau and Tianshan Mountains. In flat areas like the Tarim Basin, the sub-grid orographic variance effectively describes the feature of terrain complexity. The sub-grid orographic variance is non-negligible data for the sub-grid orographic parameterization scheme, which produces the turbulent orographic form of drag and exerts a prominent impact over mountains regions. When the height of the sub-grid terrain is relatively small and there is airflow over the mountains, the gravity wave is forced by vertical movement. Thus, gravity wave drag is propagated. When the boundary layer has stable conditions and the sub-grid terrain is sufficiently high, vertical flow is limited and the lower-level airflow around mountains cannot cross it. Airflow is forced to go around the mountain flanks, directly exchanging momentum with the surface. Flow-blocking drag is thus generated. The surface and upper-level stress (m/s^2) of integrated GWD and FBD is represented in Figure 3. The stress magnitude is derived from DUSFCG (column-integrated U component gravity wave drag stress) and DVSFCG (column-integrated V component gravity wave drag stress). Figure 3a shows that high-value stress propagated by gravity waves is mainly located at mountain edges, especially the Tianshan Mountains, Altai Mountains, and Iranian Plateau, where the terrain is flat and the stress is lower. This indicates that the stress depends on orographic variance. Figure 3b illustrates that the stress was forced only by the flow-blocking drag in the FBD simulation, which was eliminated by gravity waves breaking over the mountains at upper levels. The surface stress differences between GWD and FBD show in the Figure 3c; stronger stress (red pixels in the picture) was considerably reduced compared to the GWD (black rectangular lines). This means that the GWD has greater influence on winds fields. The stress was more obviously reflected in the upper levels. Upper-level stress was calculated by combining the DTAUX3D (local U wind component gravity drag stress) and DTAUY3D (local V wind component gravity drag stress). They were the output variables of the WRF model. From Figure 4a,b, we set the longitude–pressure vertical profile cross-section-averaged drag from the simulation of GWD and FBD over the Tianshan Mountains (Lat = 42.63° N), respectively. The vertical zonal profile selected the zonal cross-section in general. However, considering that the Tianshan Mountains are east–west, we adopted the warp cross-section here. Figure 4b shows that the sub-orographic drag generated by FBD clearly decreased in the middle-upper troposphere.

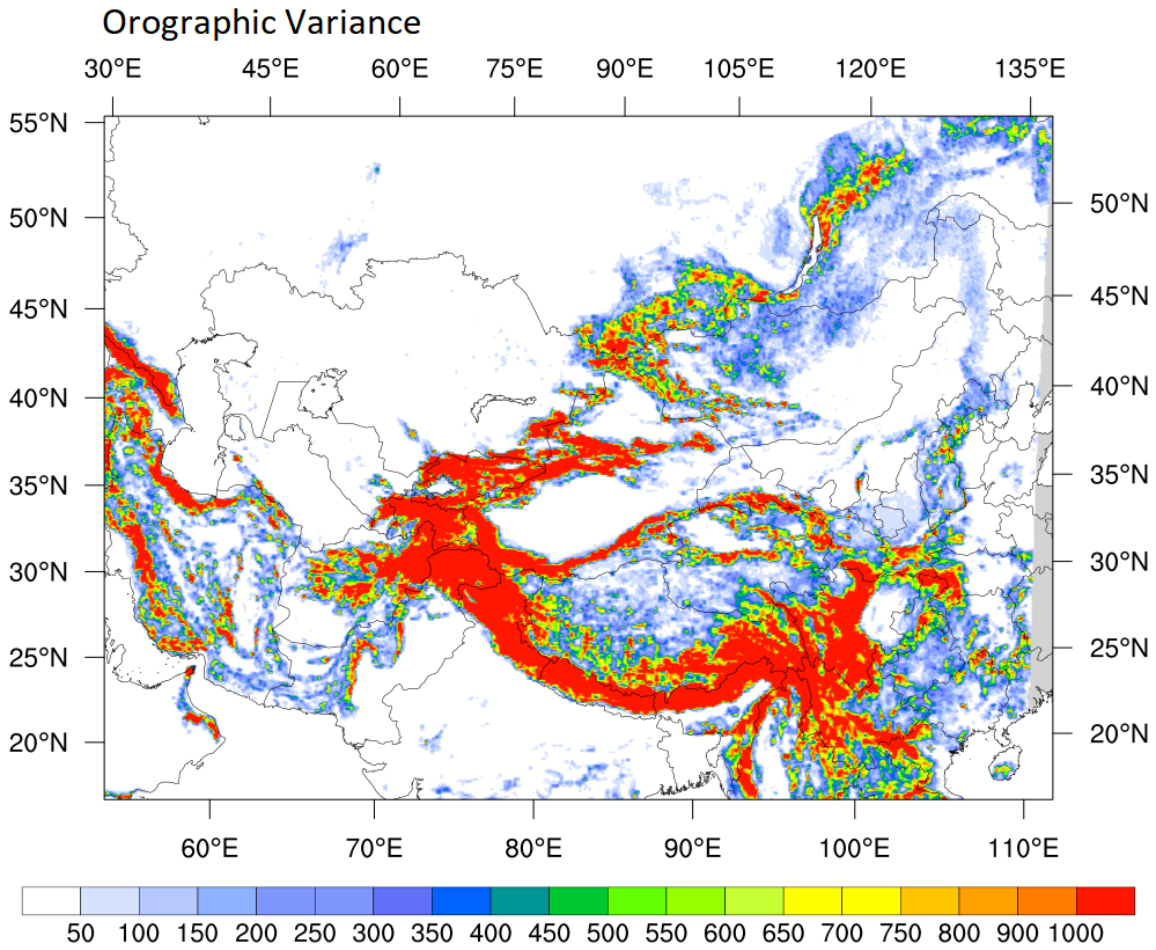

Figure 2. Central Asia sub-grid orographic variance (m) at 0.0083° resolution used in the Weather Research Forecast (WRF) calculated with U.S. Geological Survey (USGS) elevation data.

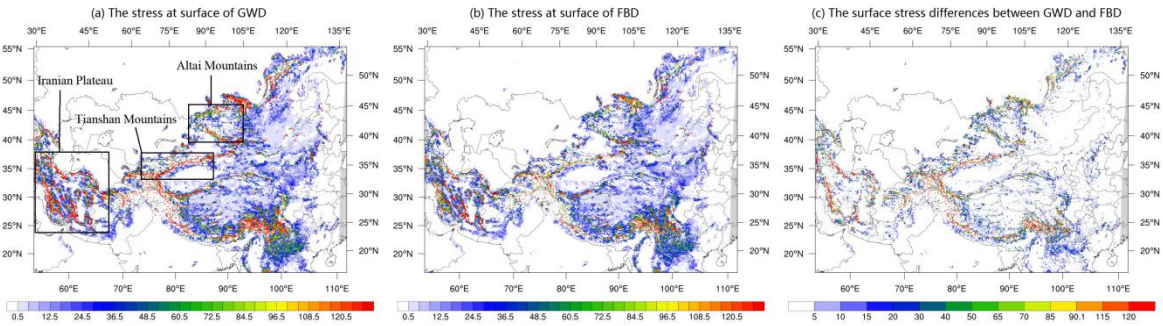

Figure 3. Sub-grid orographic drag stress at the surface of the GWD (**a**), the stress produced exclusively by flow-blocking drag (FBD) (**b**), and the surface stress between GWD and FBD (**c**), which are plotted from the column-integrated U component gravity wave drag stress (DUSFCG) and column-integrated V component gravity wave drag stress (DVSFCG) of the simulation by $(DUSFCG^2 + DVSFCG^2) \times 3600$.

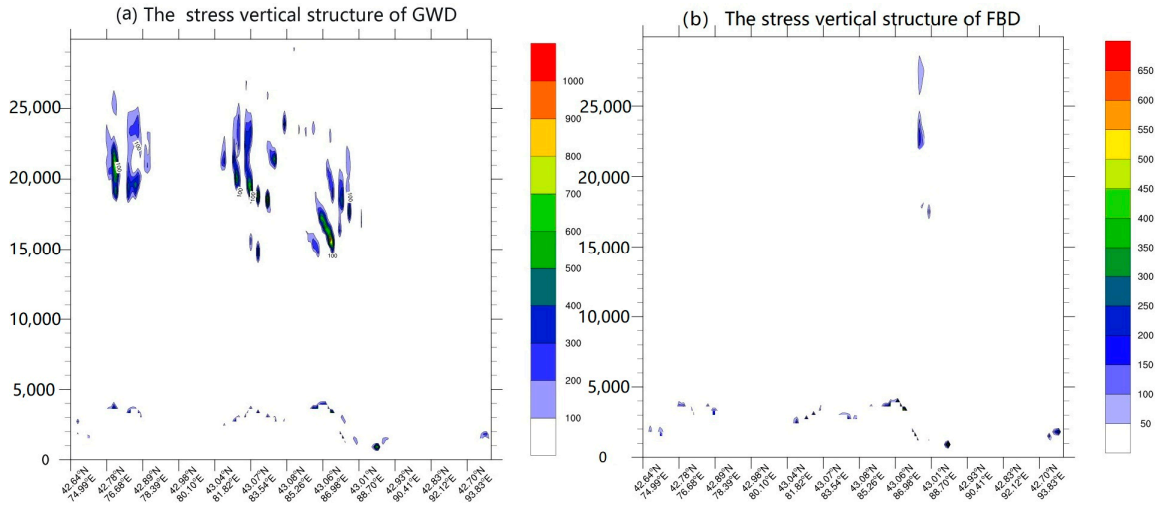

Figure 4. Longitude–pressure cross-section of the vertical structure of sub-grid orographic drag stress of GWD (**a**) and FBD (**b**) plotted from the DTAUX3D and DTAUY3D of the simulation by (DTAUX3D^2 + DTAUY3D^2) × 3600.

3.2. *Evaluation of Wind Speed and Air Temperature*

3.2.1. Ten-Meter Wind Speed

The sub-grid orographic drag directly impacts wind speed at the near-surface layer, especially where there is high orographic variance (Figure 2). Three simulations of the 10 m wind speed were evaluated by observation. The evaluation metrics are shown in Table 2. The results demonstrated that GWD and FBD significantly reduced the overestimation of 10 m wind speed. The bias of GWD and FBD was reduced by 34.39% and 32.99%, respectively, compared to the CRTL simulation, and the wind speed RMSE was reduced by 10.33% and 9.39%, respectively, compared to CRTL. This shows that the effects of sub-grid orographic drag alleviate wind speed overestimations near the surface.

Table 2. Mean bias (Bias, m/s), mean absolute error (MAE, m/s), and root mean squared error (RMSE, m/s) of wind speeds at 10 m, and statistic evaluation of hourly simulations at the station verified against surface observations.

Metrics/Cases	Bias	Δ	RMSE	Δ	MAE	Δ
CRTL	1.16	0.00	2.13	0.00	1.61	0
GWD	0.76	34.48	1.91	10.33	1.57	2.48
FBD	0.78	32.76	1.93	9.39	1.46	9.32

Δ presents the ratio of improvement (Δ = 100% ($Bias_{FBD} - Bias_{CRTL}$)/$Bias_{CRTL}$).

3.2.2. Vertical Structure of Wind Evaluation

The gravity wave breaking at upper levels propagates drag to affect the zonal wind structure. The flow-blocking drag only exerts effects near the surface. In general, the WRF can describe the structural circulation features of the zonal winds well. Figure 5a shows the isobaric wind of the average latitude–pressure cross-section (42°–43° N) over the Tianshan Mountains (Latitude = 42° N). The vertical structure wind speed of the three sets simulations, the middle-upper troposphere, and low troposphere wind speed slightly decreased by GWD compared to CRTL (black rectangular lines), and the vertical wind direction and speed changed (pink rectangular lines). The results demonstrate that the stress from the gravity wave breaking produced drag at the upper level and exerted significant impacts on the momentum flux and convective gravity wave drag centered on middle-upper levels. Figure 5b,c illustrate the differences of vertical structure wind speed between GWD and FBD, which only kept the flow blocking around the near surface. The blocking effect of the

topography decelerated the near-surface layer airflow, so the low troposphere wind reduced compared to the CRTL (red rectangular lines at the bottom left). Moreover, the middle-upper troposphere wind decreased clearly compared to GWD (black rectangles), and the vertical speed was also enhanced. The orographic block impacts the flow near the surface. Figure 6 shows the bias and RMSE of each simulation at isobaric layers. Figure 6a shows the isobaric wind speed bias of each vertical level examined by radio sounding data. GWD produced greater negative bias below 300 hPa due to the gravity waves producing drag at the upper levels when breaking. This breaks the inertial oscillation of the horizontal air flow. The simulations of the CRTL did not consider the blocking effect of near-surface winds, which have a positive deviation below 800 hPa. The FBD reduced negative deviations compared to the GWD below 300 hPa (black rectangles). The reason pertains to the flow blocked on the mountain. Air flow was blocked or flowed around the mountain flanks. This effectively slows down the wind speed. Figure 6b illustrates the RMSE of isobaric horizon winds. GWD obtained a maximum RMSE between the levels of 300 and 850 hPa. Simulations of the CRTL had the largest RMSE below 850 hPa. These results indicate that the FBD performed better than the GWD and CRTL. Flow-blocking can alleviate overestimations of wind around mountains. The recognition of the above analysis refers to the dynamic framework of the WRF model. The sub-grid orographic drag is an additional dynamic derived from the arbitrary variation of the topography. The wind speed at the upper levels has a negative deviation in the current simulation; thus, the sub-grid orographic drag should be specified.

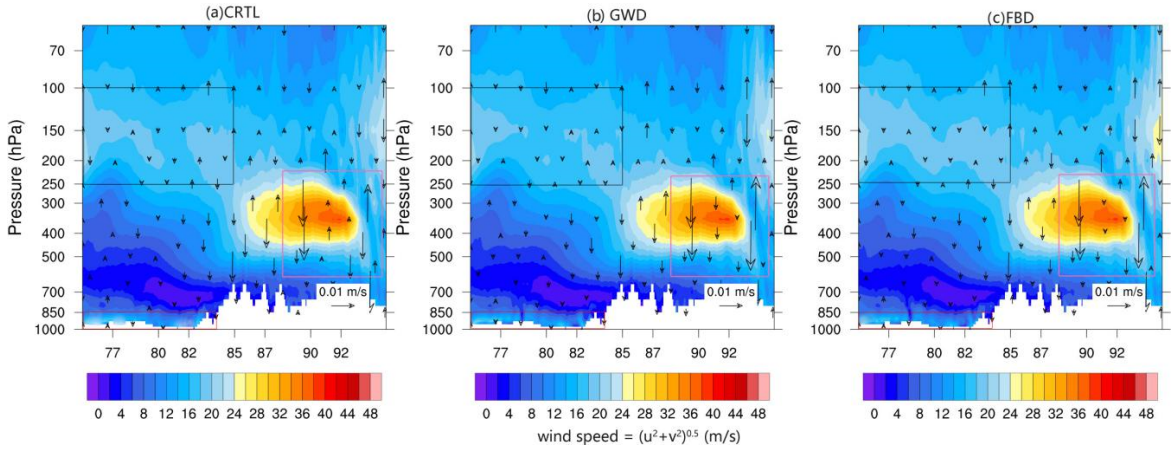

Figure 5. Latitude–pressure cross-section average of wind speed over the Tianshan Mountains (latitude = 42° N). Color represents horizontal wind speed, and the arrows represent vertical speed (**a**) for CRTL simulation, (**b**) for GWD experiment, and (**c**) for FBD simulation.

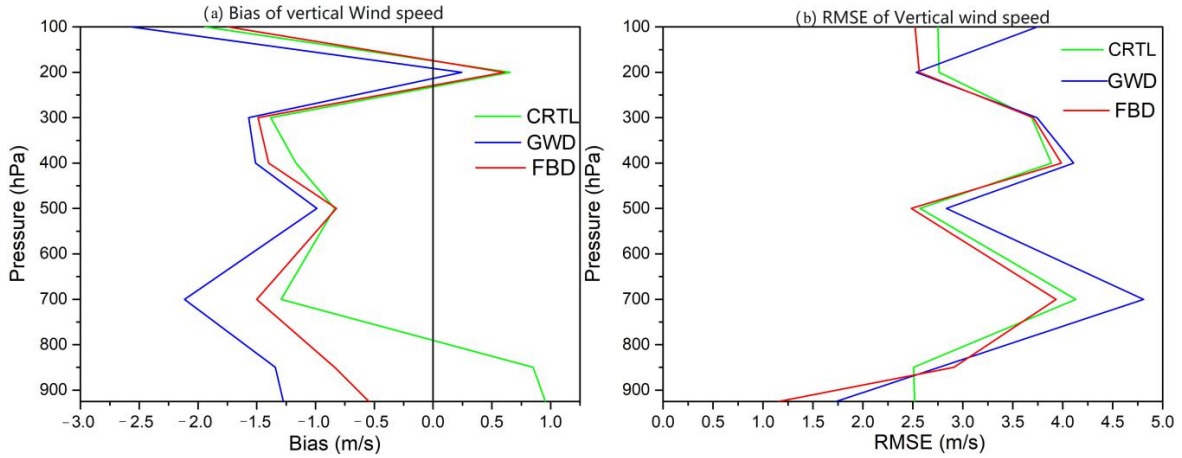

Figure 6. The Bias and RMSE of vertical wind speed examined against radio sounding data averaged hourly, (**a**) for bias of wind speed at each level and (**b**) for RMSE of wind speed at each level (green line for CRTL, blue line for GWD, and red line for FBD simulation).

3.3. Evaluation of Air Temperature and Specific Humidity

3.3.1. Two-Meter Air Temperature and Specific Humidity

The sub-grid orographic drag also indirectly impacts air temperature and specific humidity in the regional model forecast, which changes the air transport and convection through atmosphere–land interactions. The air temperature and specific humidity of three different simulations were examined against surface observations. The bias and RMSE are given in Table 3. The air temperature of all simulations was performed with systematically warm bias. The simulation of the CRTL had the largest bias, and the RMSE, GWD, and FBD show limited alleviation. The differences are not conspicuous. This may result from stable stratification with weaker convection in wintertime. Although all of the 2 m air temperature simulations were not obviously different in terms of evaluation metrics, FBD had the best performance with the smallest RMSE and mean bias. These results demonstrate that the FBD can exert indirect improvements on 2 m temperature forecasts, although the improvements are not obvious. For specific humidity, however, the three simulations had the same dry bias. This might relate to the rare water vapor over Central Asian arid land in wintertime. The GWD and FBD had the same mean absolute error. The FBD had the lowest RMSE, at 0.78 g/kg, and surface wind speed directly impacted the evaporation. Thus, FBD could indirectly change the vapor content. This illustrates that the GWD and FBD had insufficient impact on surface-specific humidity when compared to CRTL.

Table 3. The mean bias (T2-Bias, °C), mean absolute error (T2-MAE, °C), and root mean squared error (RMSE, °C) of air temperature at 2 m; the mean bias (spfh-Bias, g/kg), mean absolute error (spfh-MAE, g/kg), and root mean squared error (spfh-RMSE, g/kg) of specific humidity at 2 m; and the statistical evaluation of hourly simulations at stations verified against surface observations.

Simulations	T2-Bias	T2-MAE	T2-RMSE	spfh-Bias	spfh-MAE	spfh-RMSE
CRTL	0.28	2.64	3.79	−0.09	0.57	0.81
GWD	0.26	2.66	3.86	−0.09	0.55	0.79
FBD	0.25	2.65	3.62	−0.09	0.55	0.78

3.3.2. Vertical Structure of Air Temperature and Specific Humidity

The above analysis of wind speed simulations demonstrates that sub-grid orographic drag has a considerable influence on the wind structure in vertical isobaric layers. Additionally, the complex terrain produced sub-grid orographic drag over mountains. It changes wind fields to some degree, thus, the vertical structure pattern of air temperature and specific humidity at isobaric layers is impacted. Figure 7 shows three experiments of the latitude–pressure cross-section temperature over the Tianshan Mountains. The GWD and FBD increase between 400 to 500 hPa versus the CRTL. The stratosphere of the CRTL is colder than the others, although there is little difference between them. The turbulent kinetic energy is not sufficient in winter due to the stable atmospheric stratification. Figure 7 shows the temperature evaluation results verified by radio sounding. From Figure 7a, it is clear that the bias of temperature at 850–600 hPa reduced when compared to CRTL, and there is a cold bias from 900 to 500 hPa. All of the simulations of temperature near the surface suffer from warm bias, but they are not obviously different at other isobaric layers between 500 to 200 hPa. The temperature changed partly because of the thermal wind relationship. Wind speed affected the air flow and vertical convection. The RMSE of the three experiments is plotted in Figure 7b. The RMSE of FBD and GWD reduced slightly below 500 hPa. FBD had the smallest RMSE at the low troposphere. The bias and RMSE generally indicated that the vertical pattern of the FBD simulation better agrees with the observations than CRTL and GWD. Figure 7c,d show the bias and RMSE of the isobaric-specific humidity, respectively. The bias has nearly no difference in the three experiments. It is not useful to evaluate the impact of changing the dry or wet vertical structure of specific humidity. The difference is less than 0.1 g/kg. The RMSE illustrates that GWD and FBD perform better than CRTL. FBD shows moderate bias and the RMSE of specific humidity at the low troposphere.

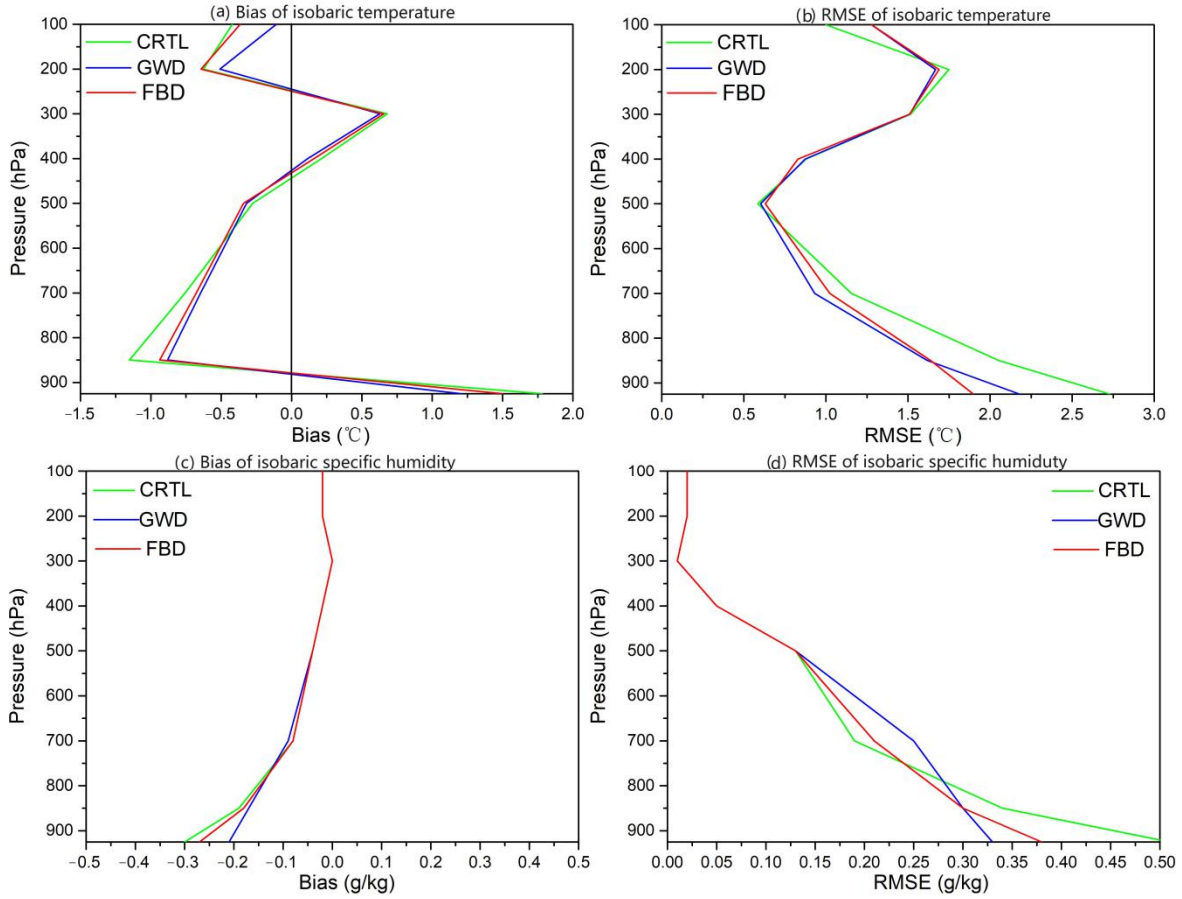

Figure 7. Vertical structure bias and RMSE of the temperature and specific humidity examined against radio sounding data over Central Asia. In each diagram, the green line denotes CRTL, the blue line is GWD, and the red line is FBD.

4. Summary and Conclusions

Wind speed is often overestimated in wintertime in Central Asia, where the terrain is complex, due to the effects of sub-grid orographic drag. Such drag is significant in winter and has stable atmospheric stratification. Because gravity wave drag parameterizations include both upper-level gravity drag and near-surface flow blocking, these two kinds of drag are considered together in the WRF model. In this study, we demerged flow-blocking drag from gravity wave drag in the WRF model. We performed three sets of numerical simulations and examinations with surface synoptic observations and radio sounding data to investigate the performance of these two kinds sub-grid orographic drag. Here, we summarize a few key points of this study:

First, we determined the distribution and features of stress near the surface and vertical structure. We found that with more variance, there is stronger sub-grid orographic drag stress. The stress at the middle-upper troposphere of the FBD (flow blocking drag stress only) reduced considerably compared to GWD. We then evaluated the performance of the surface and vertical structure wind speed, air temperature, and specific humidity. Statistical metrics showed that it is useful to reduce the positive bias of wind speed at the surface by gravity wave drag, though this causes greater negative bias of wind at the middle-upper troposphere in GWD. FBD not only reduces overestimations of wind speed near the surface, but also alleviates absolute bias at upper levels. The simulation of FBD was compared to GWD and CRTL, which were reduced by RMSE by 0.2 m/s (9.3%). Moreover, the vertical speed and direction of GWD at each isobaric layer changed considerably compared to CRTL and FBD. The stress caused from the breaking drag of gravity waves at the upper levels produced excessive large-scale circulation over mountains. This suggests that the sub-grid orographic drag should be

specified. The simulations demonstrated that flow-blocking has capacity to solve the overestimation of wind speeds over complex terrain.

A temperature evaluation showed that sub-grid orographic drag does not have a significant impact on 2 m air temperature. Both GWD and FBD improved temperature at vertical isobaric layers below 500 hPa. The slightly negative bias was alleviated via the stress from the complex terrain. In general, the air temperature at the surface and vertical isobaric slightly improved compared to CRTL. Thus, it is feasible to use FBD in regions with complex terrain. An evaluation of specific humidity indicated that sub-grid orographic drag is not sensitive to specific humidity at upper levels in winter. The RMSE reduced only slightly when compared to CRTL.

The above conclusions show that sub-grid orographic drag is effective at reducing the estimation of wind at the surface. This is superior to gravity wave breaking drag at the upper levels and other fields, such as the vertical structure of temperature and wind. Flow-blocking drag is useful for improving the performance of wind speed over complex terrain regions. In consideration of our results, we updated the FBD in the WRF model in version 3.8.1 and implemented it in the Xinjiang regional forecast operational system, RMAPS-CA (Rapid-Refresh Multiscale Analysis and Prediction System-Central Asia), to improve the performance for wind forecasts.

Author Contributions: Investigation: H.L., C.J., H.Z., J.L., J.S., J.Z., A.M., S.F.; writing and editing: H.L., C.J., H.Z., J.L., A.M., S.F. All authors have read and agreed to the published version of the manuscript.

Funding: The research was supported by the National Key Research and Development Program of China (2018YFC1507105), the National Natural Science Foundation of China (41801019, 41875023), the China Meteorological Administration's public welfare industry project (GYHY201306066) and the Research Foundation of Central Asia for Atmospheric Science (CAAS201811, CAAS202009).

Acknowledgments: We are grateful to G.X. Zhang for providing FNL data and to R.J. Liu for advice on this investigation.

Conflicts of Interest: The authors declare no conflict of interest.

References

1. Kim, Y.J.; Doyle, J.D. Extension of an orographic-drag parameterization scheme to incorporate orographic anisotropy and flow blocking. *Q. J. R. Meteorol. Soc.* **2005**, *131*, 1893–1921. [CrossRef]
2. Palmer, T.N.; Shutts, G.J.; Swinbank, R. Alleviation of a systematic westerly bias in general circulation and numerical weather prediction models through an orographic gravity wave drag parameterization. *Q. J. R. Meteorol. Soc.* **1986**, *112*, 1001–1040. [CrossRef]
3. Mesinger, F.; Wobus, R.L.; Baldwin, M.E. Parameterization of form drag in the Eta Model at the National Centers for Environmental Prediction. In Proceedings of the 11th Conference on Numerical Weather Prediction, Norfolk, VA, USA, 19–23 August 1996; pp. 324–326.
4. Whiteway, J.A.; Pavelin, E.G.; Busen, R.; Hacker, J.; Vosper, S. Airborne measurements of gravity wave breaking at the tropopause. *Geophys. Res. Lett.* **2003**, *30*. [CrossRef]
5. Sharman, R.D.; Trier, S.B.; Lane, T.P.; Doyle, J.D. Sources and dynamics of turbulence in the upper troposphere and lower stratosphere: A review. *Geophys. Res. Lett.* **2012**, *39*, L12803. [CrossRef]
6. Cai, X.; Yuan, T.; Zhao, Y.; Pautet, P.D.; Taylor, M.J.; Pendleton, W.R. A coordinated investigation of the gravity wave breaking and the associated dynamical instability by a Na lidar and an Advanced Mesosphere Temperature Mapper over Logan, UT (41.7° N, 111.8° W). *J. Geophys. Res. Space Phys.* **2014**, *119*, 6852–6864. [CrossRef]
7. Yuan, T.; Pautet, P.D.; Zhao, Y.; Cai, X.; Criddle, N.R.; Taylor, M.J.; Pendleton, W.R. Coordinated investigation of midlatitude upper mesospheric temperature inversion layers and the associated gravity wave forcing by Na lidar and Advanced Mesospheric Temperature Mapper in Logan, Utah. *J. Geophys. Res. Atmos.* **2014**, *119*, 3756–3769. [CrossRef]
8. Zadra, A.; Roch, M.; Laroche, S.; Charron, M. The subgrid-scale orographic blocking parameterization of the GEM model. *Atmos. Ocean.* **2003**, *41*, 155–170. [CrossRef]
9. Choi, H.J.; Hong, S.Y. An updated subgrid orographic parameterization for global atmospheric forecast models. *J. Geophys. Res. Atmos.* **2015**, *120*, 445–457. [CrossRef]

10. Kim, Y.J.; Arakawa, A. Improvement of orographic gravity-wave parameterization using a mesoscale gravity-wave model. *J. Atmos. Sci.* **1995**, *52*, 1875–1902. [CrossRef]
11. Hong, S.Y.; Choi, J.; Chang, E.C.; Park, H.; Kim, Y.J. Lower-tropospheric enhancement of gravity wave drag in a global spectral atmospheric forecast model. *Weather Forecast.* **2008**, *23*, 523–531. [CrossRef]
12. Jimenez, P.A.; Dudhia, J. Improving the representation of resolved and unresolved topographic effects on surface wind in the WRF model. *J. Appl. Meteorol. Climatol.* **2012**, *51*, 300–316. [CrossRef]
13. Zhang, R.; Xu, X.; Wang, Y. Impacts of subgrid orographic drag on the summer monsoon circulation and precipitation in East Asia. *J. Geophys. Res. Atmos.* **2020**, *125*. [CrossRef]
14. Wood, N.; Brown, A.R.; Hewer, F.E. Parametrizing the effects of orography on the boundary layer: An alternative to effective roughness lengths. *Q. J. R. Meteorol. Soc.* **2001**, *127*, 759–777. [CrossRef]
15. Beljaars, A.C.; Brown, A.R.; Wood, N. A new parametrization of turbulent orographic form drag. *Q. J. R. Meteorol. Soc.* **2004**, *130*, 1327–1347. [CrossRef]
16. Zhong, S.; Chen, Z. Improved wind and precipitation forecasts over South China using a modified orographic drag parameterization scheme. *J. Meteorol. Res.* **2015**, *29*, 132–143. [CrossRef]
17. Ji, Z.M.; Kang, S.C. Double-nested dynamical downscaling experiments over the Tibetan Plateau and their projection of climate change under two RCP scenarios. *J. Atmos. Sci.* **2013**, *70*, 1278–1290. [CrossRef]
18. Zoltan, T. Ensemble Forecasting in WRF. *Bull. Am. Meteorol. Soc.* **2001**, *82*, 695–698.
19. Skamarock, W.C.; Klemp, J.B. A time-split nonhydrostatic atmospheric model for weather research and forecasting applications. *J. Comput. Phys.* **2008**, *227*, 3465–3485. [CrossRef]
20. Chouinard, C.; Béland, M.; McFarlane, N. A simple gravity wave drag parametrization for use in medium-range weather forecast models. *Atmosphere* **1986**, *24*, 91–110. [CrossRef]
21. Hong, S.-Y.; Lim, J.O. The WRF single-moment 6-class microphysics scheme (WSM6). *J. Korean Meteorol. Soc.* **2006**, *42*, 129–151.
22. Kain, J.S.; Fritsch, J.M. A one-dimensional entraining detraining plume model and its application in convective parameterization. *J. Atmos. Sci.* **1990**, *47*, 2784–2802. [CrossRef]
23. Clough, S.A.; Shephard, M.W.; Mlawer, E.J. Atmospheric radiative transfer modeling: A summary of the AER codes. *J. Quant. Spectr. Radiat. Transf.* **2005**, *91*, 233–244. [CrossRef]
24. Iacono, M.J.; Delamere, J.S.; Mlawer, E.J.; Shephard, M.W.; Clough, S.A.; Collins, W.D. Radiative forcing by long-lived greenhouse gases: Calculations with the AER radiative transfer models. *J. Geophys. Res.* **2008**, *113*, D13103. [CrossRef]
25. Hong, S.Y.; Noh, Y.; Dudhia, J. A new vertical diffusion package with an explicit treatment of entrainment processes. *Mon. Weather Rev.* **2006**, *134*, 2318–2341. [CrossRef]
26. Chen, F.; Dudhia, J. Coupling an advanced land surface-hydrology model with the Penn State-NCAR MM5 modeling system. Part II: Preliminary model validation. *Mon. Weather Rev.* **2001**, *129*, 587–604. [CrossRef]